ADVANCED MATERIALS INTERFACES
Open Access
www.advmatinterfaces.de

Tuning Catalytic Activity of Ni–Co Nanoparticles Synthesized by Gamma-Radiolytic Reduction of Acetate Aqueous Solutions

Yi Yang, Pavel A. Korzhavyi, Pavel A. Nikolaychuk, Elena F. Bazarkina, Kristina O. Kvashnina, Sergei M. Butorin, Nadezda V. Tarakina, and Inna L. Soroka**

Transition metal-based catalysts show great potential to replace Pt-based material in energy conversion devices thanks to their low cost, reasonable intrinsic activity, thermodynamic stability, and corrosion resistance. The electrochemical performance of such catalysts is sensitive to their composition and structure. Here, it is demonstrated that homogeneous alloy nanoparticles with varying Ni-to-Co ratio and controlled structure can be synthesized from aqueous Ni(Co) acetate solutions using a facile γ-radiolytic reduction method. The obtained samples are found to possess defects that are ordered to form polytypes structures. The concentration of these defects depends on the Ni-to-Co ratio, as supported by the results of ab initio calculations. It is found that structural defects may influence the activity of catalysts toward the oxygen evolution reaction, while this effect is less pronounced with respect to the oxygen reduction reaction. At the same time, the activity of Ni–Co catalysts in the hydrogen evolution reaction is affected by formation of Ni—OH bonds on the surface rather than by the presence of structural defects. This study demonstrates that the composition of Ni—Co nanoparticles is an essential factor affecting their structure, and both composition and structure can be tuned to optimize electrochemical performance with respect to various catalytic reactions.

1. Introduction

Based on green and sustainable energy conversion and storage technologies, fuel cells, metal–air batteries, and water splitting devices are promising alternatives to traditional fossil fuels.[1,2] Their large-scale applications require, among others, cost-effective catalysts to increase sluggish kinetics of the hydrogen evolution reaction (HER), oxygen reduction reaction (ORR), and oxygen evolution reactions (OER), which are the key processes in the above-mentioned systems. Precious metal-based materials are best known as the most technologically relevant electrocatalysts.[3] However, the scarcity of precious metal resources and their high cost promote extensive research on replacing them with less noble catalysts.[4] Transition metal-based catalysts show great potential to replace precious metal-based catalysts due to their low cost, reasonable intrinsic activity, thermodynamical stability, and corrosion resistance in alkaline

Y. Yang, I. L. Soroka
Department of Chemistry
School of Engineering Sciences in Chemistry
Biotechnology and Health
KTH Royal Institute of Technology
Stockholm S-100 44, Sweden
E-mail: yiyan2@kth.se; soroka@kth.se

P. A. Korzhavyi
Department of Materials Science and Engineering
KTH Royal Institute of Technology
Stockholm SE-100 44, Sweden

The ORCID identification number(s) for the author(s) of this article can be found under https://doi.org/10.1002/admi.202300038.

DOI: 10.1002/admi.202300038

P. A. Nikolaychuk
Institute of Materials Science and Technology
TU Wien
Getreidemarkt 9, Wien 1060, Austria

E. F. Bazarkina, K. O. Kvashnina
The Rossendorf Beamline at ESRF—The European Synchrotron
CS40220, CEDEX 9, Grenoble 38043, France

E. F. Bazarkina, K. O. Kvashnina
Institute of Resource Ecology
Helmholtz Zentrum Dresden-Rossendorf (HZDR)
PO Box 510119, 01314 Dresden, Germany

S. M. Butorin
Condensed Matter Physics of Energy Materials, X-ray Photon Science
Department of Physics and Astronomy
Uppsala University
PO Box 516, Uppsala SE-75120, Sweden

N. V. Tarakina
Max-Planck-Institut für Kolloid-und Grenzflächenforschung
Potsdam Science Park
Am Mühlenberg 1 OT Golm, 14476 Potsdam, Germany

medium.[5,6] Among them, Ni, Co, and the bimetallic Ni–Co nanoalloys are intensively investigated and show great potential as efficient electrocatalysts for HER,[7] ORR,[8] and OER.[9] Due to the synergetic effects induced upon alloying/interface formation, the Ni–Co alloy may expose more active sites and more atomic defects; thus, leading to a significant improvement in catalyst performance.[8,10–12]

As reported in the literature, different synthesis approaches were used to obtain Ni–Co nanoalloys (both on the support and freestanding): electrochemical deposition,[13] wet-chemistry,[14] and co-reduction of Co^{2+} and Ni^{2+} salts on biopolymer templates.[15] One of the powerful tools for the production of bimetallic nanomaterials is ionizing radiation-induced reduction of metal ions in aqueous solutions.[16–19] The main advantage of this method is the possibility to precisely control the amount of strong reducing species homogeneously distributed in solution; and thus, to govern the conversion yield of final products. Another advantage is that one can produce nanomaterial in situ both freestanding and on different types of supports; the latter is especially useful for designing materials for catalysis applications.[20,21] The ionizing radiation induced synthesis of monometallic nanoclusters from aqueous solutions of metal precursors consists of several steps, including reduction of metal ions, atoms coalescence into clusters, adsorption of the excess of metal ions on the surfaces of metal clusters, and formation of stable aggregates.[19,22] Bimetallic clusters of different composition and morphology can be obtained by irradiation of a mixture of two ionic precursors by alternating the synthesis parameters. Thus, it was demonstrated that by varying irradiation dose rates, one can tune the morphology Ag–Au cluster from core–shells (at low dose rates) to alloys (at high dose rates).[18,23] In another study Ag/Pd nanoclusters with high aspect ratio were obtained by changing dose rates, types of surfactants, and complexing agents.[24] Important parameters which need to be considered for the successful synthesis of bimetallic clusters out of aqueous solutions are reduction potentials of the constituent ions.[25] As noble metals ions are readily reduced and remain stable in solutions, radiation induced syntheses of mainly noble metal based bi- and multimetallic clusters, such as Ag–Au,[23] Ag–Cu,[16] Cu–Pd,[17] Au–Pd,[26] Au-Sn,[27] Ag-Ni,[28] Pd-Ni,[29] and some others[18] were reported in the literature. Radiation induced synthesis of non-noble metallic nanomaterials remains challenging due to backward reactions (oxidation) which may occur in solutions during the irradiation and/or under the post-irradiation treatment.[30] Thus, in our previous work, we synthesized freestanding Ni nanoclusters by radiolytic reduction of Ni^{2+} in an aqueous precursor solution.[30] Although the reduction conditions of the synthesis were created, the metallic Ni was partially oxidized so that the nanoclusters were covered with $Ni(OH)_2$/NiO layers. The combination of Ni with less noble metals and the formation of bimetallic compounds may decrease the Ni oxidation during the synthesis. In case a mixed solution of two non-noble ionic precursors is irradiated under reduction conditions or chemically reduced, both ions have an equal probability to be reduced. However, further electron transfer from less noble atoms (for example Co) to more noble metal ions (Ni) may favor the reduction of the latter.[19]

It is known that the structure of Ni–Co alloys depends on their composition. Ni–Co equilibrium binary phase diagram reveals that, at room temperature, Co rich alloys with ≤25 at% of Ni possess hexagonal close-packed (*hcp*) structure, while those with ≥25 at% Ni have face-centered cubic (*fcc*) structure, and at a temperature above 700 K, phase transition from *hcp* to *fcc* occurs for pure cobalt.[31] Meanwhile, as shown in the literature, the relation between the Ni–Co alloys composition and their crystallographic structures may deviate from the equilibrium one and depends on the shape and size of the obtained materials. Thus, electrodeposited Ni–Co alloy films of ≈50 µm thick demonstrate *fcc*, the mixture of *fcc* + *hcp*, and *hcp* structures at Co contents of 0–49 wt%, 50–80 wt%, and 81–100 wt%, respectively.[32] In the other work, it was revealed that by varying Ni-to-Co ratio, one can tune the density of defects (twins) at the surface of the bimetallic cones.[33] It is obvious, taken together, composition, structure, and morphology of Ni–Co alloys affects their physical and chemical properties.[34–37]

The aim of the current study is to reveal the effect of the composition of Ni–Co nanoalloys, obtained by ionizing radiation-induced reduction method, on their structural, chemical, and electrochemical properties. Ni–Co nanoalloys with various Ni-to-Co ratios from a mixture of Ni^{2+} and Co^{2+} acetate solutions are fabricated. Commercial carbon, Vulcan XC-72, is used as supporting material for those samples whose catalytic activity is being studied.

2. Results and Discussion

2.1. Radiation-Induced Synthesis of Metallic Co, Ni, and Alloy Ni–Co Nanoparticles in Aqueous Solutions, G-Values, and Particle Formation Pathway

When ionizing radiation interacts with water, part of its energy is absorbed and the active species (e_{aq}^-, $H^\bullet$, $OH^\bullet$, H_2O_2, and others) are produced.[38] The unit of absorbed energy is 1 Gy = 1 J kg^{-1}. One of the characteristics of the active species is G-value. G-value is the number of species produced per unit of energy absorbed by matter. G-values for the products of water radiolysis depend on types of radiation and are varied for different species. Thus, if radiolysis of neutral water is caused by γ-irradiation (or fast electrons), G-value for the solvated electrons is the same as for $OH^\bullet$ radicals and equals 0.28 µmol J^{-1}. Adding isopropanol (IPA) as a radical scavenger ensures converting OH radicals to reducing species, $(CH_3)_2COH^\bullet$; thus, increasing the G-value for the reducing species twice, to 0.56 µmol J^{-1}.[19] At the same time to reduce di-valent ions, Me^{2+}, two reducing species are required, which means that the maximum possible G-value for Me formation is 0.28 µmol J^{-1}.

Ionizing radiation induced synthesis of metallic clusters includes the reduction of the metal ions precursors in solutions by reducing agents. This process is followed by nucleation, growth, and sedimentation of the solid precipitate. The synthesis procedure is schematically illustrated in **Figure 1**a. Obviously, to reduce di-valent ions, two reducing species are required. As was suggested in our previous studies, the reduction of Ni^{2+} to atomic nickel occurs in two steps via the formation of Ni^+ intermediates.[30] Moreover, Ni^+ undergoes

ADVANCED MATERIALS INTERFACES
Open Access
www.advmatinterfaces.de

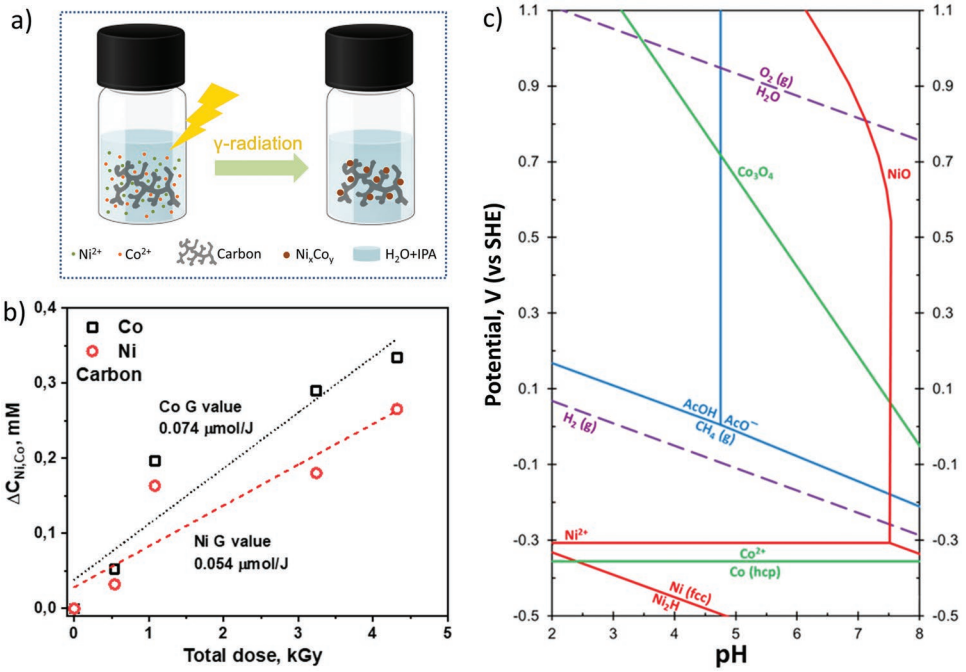

Figure 1. a) Schematic representation of the synthesis of Ni–Co/C catalysts. b) The difference between the initial and final concentrations of Co^{2+} and Ni^{2+} ions in precursor solutions with Vulcan XC-72, as a function of the total irradiation doses. The measurements are performed on a mixture of Ni and Co acetate solutions with equal initial concentrations, 2.25 mM each. The G-value for Co^{2+} and Ni^{2+} reduction calculated from the corresponding slopes is denoted on the graph. c) Potential–pH diagram of the Ni–Co–CH_3COOH–H_2O system at the temperature 298.15 K; the air pressure is 1 bar and the composition ratio of nickel and cobalt in the solution is equal to 1.

disproportionation to Ni^{2+} and Ni^0. We expect that the reduction of Co^{2+} may occur in a similar way. The tabular value of the standard reduction potentials Ni^{2+}/Ni^0 and Co^{2+}/Co^0 are close to each other and equal to −0.257 and −0.28 V, respectively.[39] As it has been mentioned above, the radiolytic formation of alloy clusters from metal ions precursors in solutions occurs via electron transfer from the less noble to more noble metal atoms, which favors the reduction of more noble metals. At the same time, it is expected that in the Co–Ni system, the probability to be reduced by the radicals for less noble and more noble metal ions is equal. Thus, the number of reduced ionic species, in general, depends on the concentration of the corresponding precursor. This is supported by the results presented in **Table 1**, where concentrations of the metal (Co, Ni) ions in the precursor solution before the irradiation and compositions of the final product, determined using ICP-OES, are shown.

As seen in the table, the experimental conversion yields of Co^{2+}(Ni^{2+}) to Co(Ni) are smaller than the theoretical one. Note, the total irradiation dose is established in such a way that 100% of Co(Ni) ions in precursor solutions is converted to metal atoms. The theoretical yield is calculated considering the G-value of reduction species formation, 0.56 μmol J^{-1}. The discrepancy between calculated and experimental conversion yield can be attributed to the following: i) backward processes (oxidation, dissolution) may occur during the synthesis; ii) a certain amount of solid Ni and Co can be lost (not fully dissolved in acid and filtered out) when preparing probes for ICP-OES analysis; and iii) the activity of carbon black toward solvated electrons and hydroxyl radicals.[40]

Another observation is that the Ni^{2+} to Ni conversion yield (11%) in Ni/C samples is significantly smaller than that of Co (70%) in Co/C one. At the same time, the conversion yield for Ni is significantly increased in the alloy samples. It may indicate that the backward reactions of nickel in solution are somehow inhibited by the presence of cobalt, and Ni reduction becomes favourable. Thus, as it was observed in our previous study,[20] metallic Ni obtained as a result of radiolytic reduction in aqueous solutions, may further oxidize to form soluble

Table 1. The amount of Ni and Co in the precursor solutions and in the final products determined with ICP-OES.

Sample ID	Initial amount of Ni^{2+}/Co^{2+} in solutions [mM]	Amount of Ni/Co converted to the solid state [mM]	The relative amount of the converted Ni/Co [wt%]	Ni-to-Co ratio in a solid sample	Ni + Co content in Vulcan XC-72 [wt%]
Ni/C	5.5	0.62	11	–	2.27
Ni_3Co/C	4.125/1.375	1.75/0.69	42/50	2.5/1	8.86
NiCo/C	2.75/2.75	0.93/0.82	34/30	1/0.9	6.37
$NiCo_3$/C	1.375/4.125	1.06/3.06	77/74	1/2.9	14.96
Co/C	5.5	3.88	70	–	14.12

ADVANCED MATERIALS INTERFACES
Open Access
www.advmatinterfaces.de

$Ni(OH)_2$. At the same time, metallic cobalt may partially oxidize to insoluble Co_3O_4. In the alloy, cobalt oxide may serve as a protective layer to either prevent the oxidation of metallic Ni or the dissolution of nickel compounds.

To understand the Ni–Co alloy formation through γ-radiation induced processes, G-values for both metals in a mixture of Ni and Co precursors solutions (Ni to Co ratio is 1) were measured. In Figure 1b, the difference between the initial and the final concentrations of cobalt and nickel ions in solutions containing Vulcan XC-72 is plotted as a function of the total irradiation dose. The slopes on the graph correspond to G-value for Ni^{2+} and Co^{2+} reduction in a mixture of Ni, Co acetate aqueous solutions with carbon powder. As seen in the graph, the total G-value for both metals is 0.128 μmol J^{-1}, which is twice as low as the theoretical value. At the same time, G-value for Co is ≈1.4 times higher than for Ni, indicating that under the current conditions, the formation of cobalt is slightly preferable. The same trend in Co and Ni G-values is observed in the 50/50 CoNi sample (NiCo) that does not contain carbon (Figure S1, Supporting Information).

To better understand the processes occurring in aqueous Ni–Co precursor solutions, chemical and electrochemical equilibria in the Ni–Co–CH_3COOH–H_2O system were calculated for $T = 298.15$ K, air pressure 1 bar, and Ni-to-Co ratios in solution equal to 1. The corresponding potential-pH diagram is shown in Figure 1c. The calculation details are given in the Supporting Information. Note, the diagrams for different Ni-to-Co ratios in the solution (3: 1 and 1: 3) are very similar because the difference in the thermodynamic activities (see Table S1, Supporting Information) results in very small changes in equilibrium pH values (±0.02) and electrode potentials (±0.005 V). Note, the experimental pH of the precursor solutions changes from 7 to 5.5 during the synthesis. As seen in the figure, the equilibrium stability of Ni ions is dependent on solution pH. Thus, as pH increases, the reduction potential of Ni^{2+}/Ni^0 decreases and the formation of Ni oxide becomes preferable. Thus, Ni^{2+} may partially exist in a form of a dispersion of Ni oxide/hydroxide in solution, and its reduction may be complicated. Meanwhile, Co ions remain thermodynamically stable at the whole pH range used in the current study. Considering the above, we suggest that during the synthesis, the reduced Co forms nucleation clusters; consequently, the solution around the Co nucleus becomes Ni-enriched. Thereafter, Ni ions are adsorbed on the Co surface and their further reduction occurs by the electron transfer from Co. This way, cobalt serves as a support and promotes nickel formation in solution upon γ-radiation induced synthesis.

2.2. Structure and Composition

2.2.1. XRD Studies

The structure of the obtained nanoparticles is investigated using XRD and (scanning) transmission electron microscopy. The XRD patterns recorded from Ni–Co/C samples with different Co-to-Ni ratios are shown in **Figure 2**. As seen in the figure, the XRD pattern from Co/C represents peaks whose positions correspond to those from both *hcp* and *fcc* Co.[41] Although some XRD peaks from these two structures overlap, positions of peaks 1 and 3 correspond solely to *hcp* Co ((100) and (101) planes), while peak 4 is characteristics for (200) plane in *fcc* Co.[41] At the same time, the relative intensities of XRD peaks shown in Figure 2 are different from those found in the reference for a powder diffraction pattern for *hcp* Co, where 100% intensity is subscribed to (101) peak. In our case, the maximum intensity corresponds to peak *2*, which position agrees with (002) and (111) planes in *hcp* and *fcc* Co, respectively. A similar XRD pattern is observed for $NiCo_3$/C and even for NiCo/C. Although, the intensities of peaks 1 and 3 tend to decrease with increasing Ni concentration, and last, these peaks resemble shoulders to the main peak in the XRD pattern for NiCo/C sample.

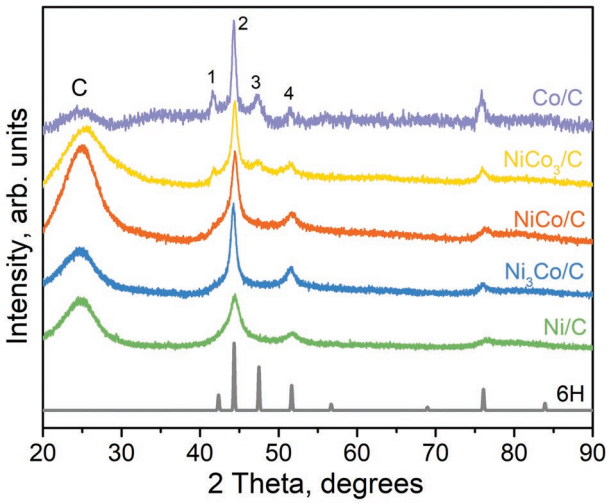

Figure 2. XRD patterns of Ni_xCo_y/C samples which have different Co-to-Ni ratios. The calculated XRD pattern of 6H polytypic structure is also included in the graph and schematically illustrated on the right side. The XRD peak labelled with "C" belongs to amorphous carbon.

The XRD patterns for Ni-rich samples correspond to those for *fcc* Ni. Note, the XRD patterns for the corresponding Co–Ni nanoparticles produced without carbon support (see Figure S2, Supporting Information) resume the same trend; thus, indicating that carbon support does not affect the structure of the studied nanoparticles. The variation of the relative intensities in the XRD patterns points out the fact that the structure of the above-mentioned compounds can probably not be a simple mixture of *fcc* and *hcp* modifications but long-period polytype crystals or extended defect areas.[42]

Although Ni and Co have both *fcc* and *hcp* allotropies, at ambient conditions, *hcp* Co and *fcc* Ni are found to be the most stable ones. In addition, it is known that bulk Ni–Co alloys possess *fcc* structure when the Ni concentration in the alloy exceeds 25%.[31] The values of lattice parameters of Ni and Co close-packed structures are close to each other (*fcc*: a_{Co} = 3.554 Å; a_{Ni} = 3.540 Å. *hcp*: a_{Co} = 2.514 Å, c_{Co} = 4.105 Å; a_{Ni} = 2.622 Å, c_{Ni} = 4.321 Å).[41,43] Thus, it is expected that the substitution of Ni(Co) in Co(Ni) lattices gives a minor contribution to the change in interatomic distances of Ni–Co alloys. Indeed, although; the composition of the samples presented in the current study varies a lot, no significant shift of the XRD peaks is observed on the X-ray diffraction patterns.

ADVANCED MATERIALS INTERFACES
Open Access
www.advmatinterfaces.de

2.2.2. TEM Studies

Overview and high-resolution TEM (HRTEM) images of all five samples are shown in **Figure 3**. One can see that in every sample, the particles can be divided into two fractions based on their size: i) small particles (1–3 nm) tightly incorporated into the carbon support and ii) large clusters (10–40 nm) distributed on the carbon support. The size distribution histograms of nanoparticles in the studied samples are also shown in Figure S3, Supporting Information. As for most samples, the signal on SAED patterns is dominated by the contribution from the carbon, it is rather difficult to distinguish between the *hcp* and *fcc* phases. To solve this problem, we performed detailed analyses of the HRTEM images of separate particles and corresponding fast fourier transformations (FFTs).

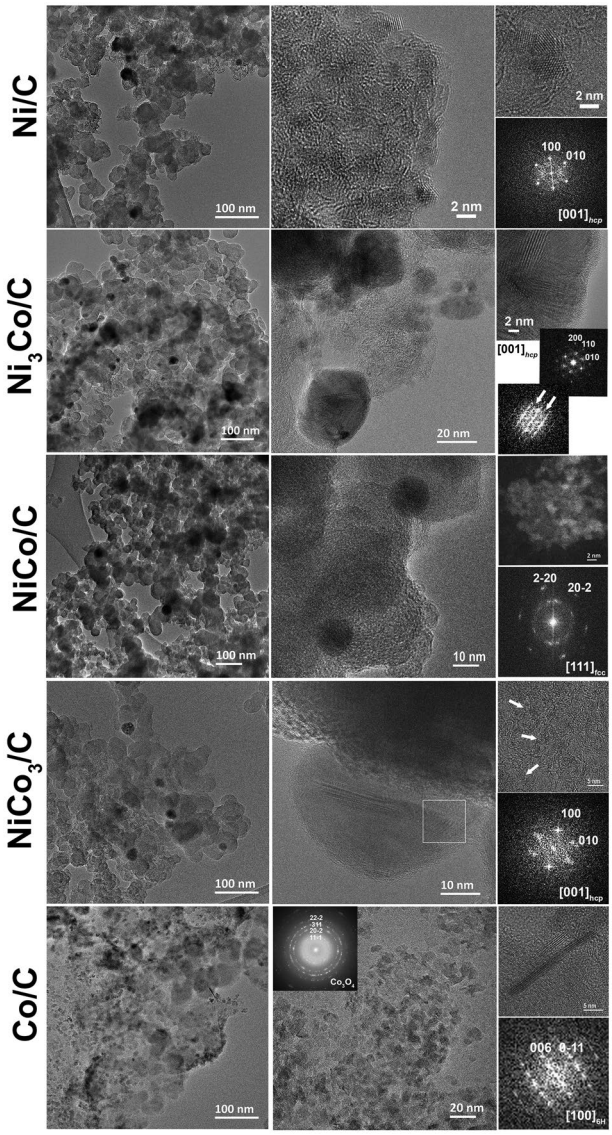

Figure 3. TEM images of Ni/C, Ni_3Co/C, NiCo/C, $NiCo_3$/C, and Co/C samples. Each row shows an overview image of nanoparticles supported on carbon, followed by HRTEM images of specific particle fractions with corresponding FFTs. Detailed descriptions of the particle fraction and the FFT analysis are given in the text.

One can see that in all samples, both *hcp* and *fcc* particles or domains within particles are found. Although we have not found a correlation between the structural type and the size of the particles, we can see that the large particles contain a lot of stacking faults. They are clearly visible on HRTEM images and appear as diffuse scattering lines or extra spots on the FFTs. In most cases, FFTs from larger particles are impossible to index because they consist of contributions from differently oriented domains of 2–3 nm in size. Figure 3 shows two FFTs obtained from different areas of the same particle in the Ni_3Co sample. The first FFT can be described as a projection along the [001] direction in the *hcp* structure, while the other is similar to a projection along the [100] direction in the *hcp* structure with broad diffuse lines and extra rows of spots marked by arrows.

The HRTEM image taken from a large particle in $NiCo_3$ sample shows similar defects. At the same time, small particles are found to be uniformly incorporated in the carbon matrix. Figure 3 (in the first and second columns) shows examples of small particles from Ni, Ni_3Co, NiCo, and $NiCo_3$. There are areas in the CoNi sample where these small particles are connected to each other. In addition to small and large particles, we found the presence of needle-like particles in the Co sample. They cannot be attributed either directly to *hcp* or *fcc* lattices or to Co oxide; we assume that most probably this is some kind of supercell/or a polytype similar to prolonged defect areas in the mixed Ni–Co samples.

2.2.3. Oxidation State

The XPS studies performed on Ni/C, Co/C, and NiCo/C samples revealed the presence of some oxidized Ni and Co at the surfaces (Figure S4 and Table S1, Supporting Information). Note that metal surfaces are quite reactive at ambient conditions; and therefore, it is very difficult to avoid oxidation.[30] The oxidation on the surface is also confirmed by the STEM analysis combined with EDX (**Figure 4**a). One can see that the layer of lower contrast is present around the large particle. It is less than 2 nm thick.

The oxidation state of cobalt nanoparticles has been further studied using XAS and XES measurements. Figure 4b displays the HERFD-XAS spectra at the Co K edge of the Co nanoparticles (freestanding and supported on carbon) which are compared with the spectrum of the Co foil. The spectral structure at ≈7712 eV in the Co K HERFD-XAS, which is characteristic of Co metal is also present in the spectra of freestanding Co NP and Co/C NP samples. However, the relative intensity of this structure decreases for the freestanding Co NP sample and becomes the lowest for Co/C. At the same time, the structure at ≈7726 eV grows up and becomes the most intense for the Co/C sample. The latter structure is associated with Co(II) oxide[44,45] and indicates a formation of oxidized NPs, being more significant for the Co/C sample. On the other hand, the Co K HERFD-XAS spectra of the freestanding Co NP do not show a broad structure at ≈7775 eV, characteristic of stoichiometric CoO.[44,45] A dissipation of this structure which rather has the multiple-scattering origin suggests that the formed oxidized Co NPs are highly defective and can be even amorphous.

ADVANCED MATERIALS INTERFACES
Open Access
www.advmatinterfaces.de

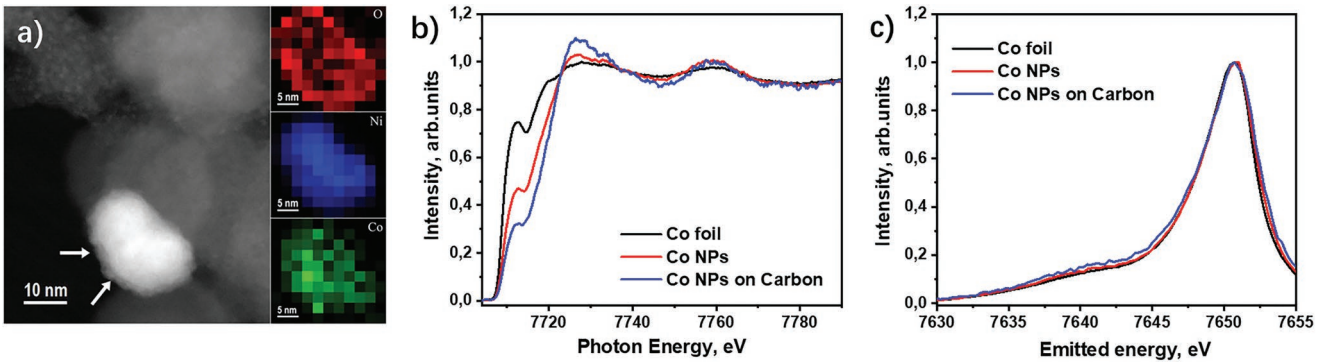

Figure 4. a) ADF-STEM images of the NiCo/C sample, showing carbon with small and large particles of a Ni–Co alloy. Arrows point to the layer of weaker contrast around the large particle, indicating its oxidation on the surface (left); EDS maps (right) of O–K; Ni–Kα, and Co–Kα signals obtained from the large particle confirm that it is oxidized on the surface. b) Co K HERFD-XAS recorded at the maximum of the main peak of K$\beta_{1,3}$ emission spectrum and c) Co K$\beta_{1,3}$ XES spectra of Co nanoparticles (NPs) both freestanding and on carbon (Vulcal-XC 72) support and Co foil, used as a reference.

The existence of the Co(II) fraction in the NP samples is also supported by the results of the Co K$\beta_{1,3}$ XES measurements (Figure 4c). Although the Co K$\beta_{1,3}$ XES maximum of the NP samples coincides with that of Co metal, the spectra of the NP reveal some asymmetric broadening on the high-energy side, being more prominent for Co/C NPs. The formation of the oxidized Co NPs is expected to cause such a high-energy broadening because the Co K$\beta_{1,3}$ XES line of CoO has a high-energy chemical shift of ≈1 eV as compared to that of Co metal.[44] At the same time, the Co K$\beta_{1,3}$ XES line is broader than that of Co metal due to electron–electron correlation effects in CoO. Therefore, the partial contribution of the Co(II) fraction to the Co K$\beta_{1,3}$ XES line of the NP samples can be the reason for its observed broadening (Figure 4c).

2.2.4. Structural Defects

As follows from the structural analysis, the studied samples contain defects, mainly in the form of stacking faults. The presence of structural defects is one of the factors that may influence the electrochemical performance of the catalysts.[46] The most frequently appearing defects are vacancies, dislocations, stacking faults, and so on. Polytype can be considered as a defect as well. Polytype structures are built up by stacking layers derived from the close-packed units. These units may consist of either one or several atoms. The stacking layers are arranged in such a way that the final long-period crystal unit cell has still a dense packing. Likewise, the most common structures, such as *hcp* and *fcc* can be described using "polytype" terminology. As shown in the literature, the polytypic structures were observed in layered structures grown from solution, vapor, melt, or gel. The origin of polytypes was attributed to different factors, such as the presence of dislocations and/or impurities, the influence of lattice vibrations, and thermodynamic factors.[47] Cumulative diffraction patterns of Co/C sample were taken as a model when by iterating over different polytypes, the final structure 6H[48] that consists of 6 stacking layers in series ABACBCA, was established. The calculated XRD pattern characteristics for the 6H structure having parameters $a = b = 2.50$ Å, $c = 12.25$ Å, are plotted in Figure 2.

To further elucidate the effect of composition on structural parameters of Ni–Co alloys, the relative stability of four close-packed lattices with different stacking of layers was studied by first-principles calculations using the exact muffin–tin orbital (EMTO) method.[49,50] The calculation details are provided in the Supporting Information. The free energy of formation, calculated for random Ni–Co alloys on the four crystal lattices relative to the standard states of Co(*hcp*) and Ni(*fcc*), is plotted in **Figure 5**a. The calculations show that Co-rich and Ni-rich alloys inherit the crystal structures of the pure elements, while for concentrated alloys in the range from ≈30 at% to ≈60 at% Co, a mixture of *fcc* and *hcp* solid solutions of the respective concentrations has the lowest free energy. In that interval, the four polytypes (with periodic stacking sequences ...[AB]... for 2H, ...[ABC]... for 3C, ...[ABAC]... for 4H, and ...[ABCACB]... for 6H) are very similar in energy; so that, even slight deviations from the thermodynamic equilibrium may stabilize one or another structure.

Due to the proximity in the energy of the different polytype structures in the range 30–60 at% Co, the formation energies of stacking faults and twins are expected to be very low. We evaluated twin boundary energy from the calculated energies F using the axial next-nearest neighbour Ising (ANNNI) model[51] as $\Delta F_{\mathrm{TB}}^{\mathrm{form}} = \pm[2F(2\mathrm{H}) - F(3\mathrm{C}) - 4F(4\mathrm{H}) + 3F(6\mathrm{H})]/A$, where the + (−) sign applies to a twin boundary in the *fcc*(*hcp*) structure and A is the area per atom in a close-packed atomic plane (at the calculated equilibrium volume). The stacking sequence of close-packed planes near the twin boundaries is as follows, *fcc*: ...ABCABCACBACBA... and *hcp*: ...ABABABACACACA... (the twin boundary plane is underlined). As Figure 5b shows, the $\Delta F_{\mathrm{TB}}^{\mathrm{form}}$ is very low in the range where the *fcc* and *hcp* structures are competing in energy, nearly vanishing for the $Ni_{0.42}Co_{0.58}$ alloy composition. Interestingly, the energy of a twin boundary in pure ferromagnetic Co is also calculated to be as low as 11 mJ m^{-2}. In the ANNNI model, this low energy value results from a frustration caused by the competing nearest, next-nearest, and next-next-nearest layer interactions. To compare with the experimental XRD results, we have computed the

ADVANCED MATERIALS INTERFACES
Open Access
www.advmatinterfaces.de

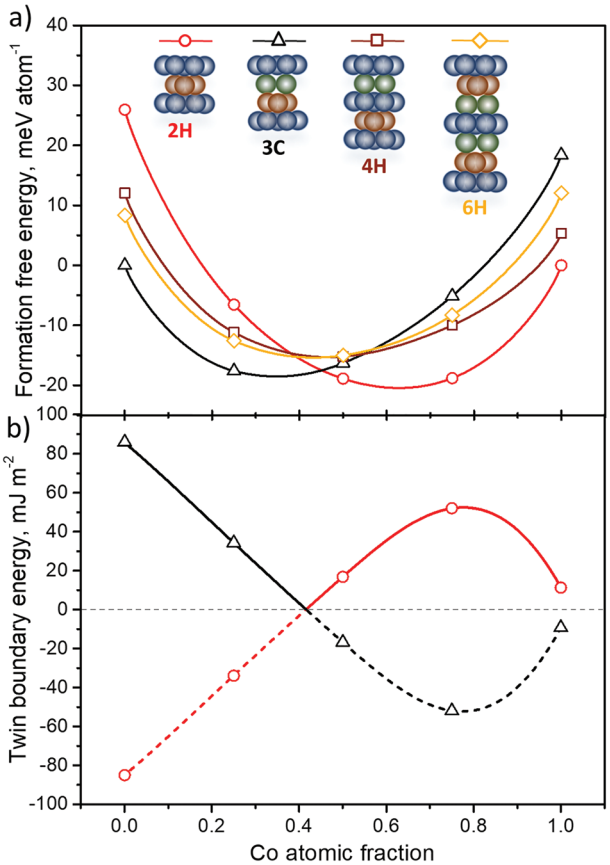

Figure 5. a) Calculated free energy of formation, at 300 K, for random alloys on the four considered lattices: 2H, 3C, 4H, and 6H. b) Calculated twin boundary energy for the two most stable structures, 3C (*fcc*) for Ni-rich and 2H (*hcp*) for Co-rich alloys. The legend applies to both panels. Symbols are calculated and lines are interpolated values; negative twin boundary energies are shown with dashed lines.

lattice parameters for the 3C and 6H polytypes, now optimizing the c/a ratio for the hexagonal polytype. The comparison is made in **Table 2**, and a good agreement is found.

In summary, the structural analysis reveals that the studied Ni–Co samples consist of two fractions of the crystalline metallic (Co, Ni, or Co–Ni) particles with the sizes of 1–3 nm and 10–40 nm. The particles surfaces are covered with the oxides of the corresponding metals. As follows from ab initio calculations and confirmed by XRD and TEM studies, all samples have close-packed structures with structural defects in the form of stacking faults.

Table 2. Comparison of calculated and measured lattice parameters of 3C and 6H polytype structures of selected Ni–Co alloys.

Polytype structure	Parameter	Experiment	Calculation
Ni (3C)	α,Å	3.54	3.527
Co (3C)	α,Å	3.54	3.525
Ni_1Co_1 (6H)	α,Å	2.5	2.496
	c,Å	12.25	12.2
	c/α	4.9	4.89

2.3. Trifunctional Electrocatalysis Toward Hydrogen Evolution, Oxygen Reduction, and Oxygen Evolution Reactions

Electrochemical performance and activity of the obtained Ni–Co catalysts toward HER, ORR, and OER are investigated. The results are shown in **Figures 6** and **7**.

2.3.1. HER

Electrochemical performance of Ni–Co nanoparticles toward hydrogen evolution reactions is shown in Figure 6a–c. Linear sweep voltammetry (LSV) curves (Figure 6a) were recorded from –1.0 to 0 V (vs RHE). As shown in Figure 6c, the Ni/C catalyst exhibits outstanding HER catalytic performance with low E_{J10} (potential boosting the current density to 10 mA cm^{-2}) equal to –0.37 V, which is higher than that for Co/C (–0.41 V) and significantly higher compared to bimetallic samples. The onset potential (E_{Onset}) of the catalysts shows a similar trend as E_{J10}, confirming that the monometallic catalysts have better performance than the bimetallic ones (Figure 6c). The Tafel slope values of the catalysts are found to vary a lot depending on the composition. (Figure 6b). Thus, Co/C sample shows the lowest slope value, of 137 mV dec^{-1}, while the Co or Ni enriched samples, $NiCo_3$/C, and Ni_3Co/C, have the highest slope values, close to 180 mV dec^{-1}. It is widely accepted that Tafel slopes of 120, 40, and 30 mV dec^{-1} correspond to a rate-determining step (RDS) of the Volmer, Heyrovsky, and Tafel steps, respectively.[52,53] In our case, although some of the samples show a larger Tafel slope close to 180 mV dec^{-1}, it is still believed that all the five studied catalysts have a Volmer step as the RDS.

2.3.2. ORR

The ORR performance of the catalysts was studied using a rotating disk electrode (RDE) where different rotating speeds could be applied to control the O_2 diffusion efficiency. The ORR polarization curves obtained at 1600 rpm are shown in Figure 6d. As seen in the figure, ORR performance of the NiCo/C catalysts, estimated from the onset potential (E_{onset} = 0.78 V) and half-wave potentials ($E_{1/2}$ = 0.65 V), is the highest among the five studied catalysts. It indicates that NiCo/C possesses superior ORR activity. It should be noted that Ni_3Co/C displayed the same E_{onset} and $E_{1/2}$ as NiCo/C, but the former has a bit lower limited current density. Based on the Koutecky–Levich (K–L) equation,[54] the electron transfer number (n) for the catalysts is calculated (Figure S6, Supporting Information). The n values for all five catalysts are found to be close to 3 (Figure 6f), implying the unremarkable ORR catalytic efficiency of the studied catalysts. This result is consistent with ORR performance of the commercial carbon supported Ni–Co catalysts.[55] The ORR kinetics of the catalyst was evaluated from the Tafel slope. The calculated slope value is commonly used as an indicator for the reaction pathway and the rate-determining step (RDS).[56] As shown in Figure 6e, the absolute values of the Tafel slopes for all five catalysts are quite close to each other and are ≈70 mV dec^{-1}. This may indicate all the catalysts have the first electron transfer as the RDS.[57]

ADVANCED MATERIALS INTERFACES
Open Access
www.advmatinterfaces.de

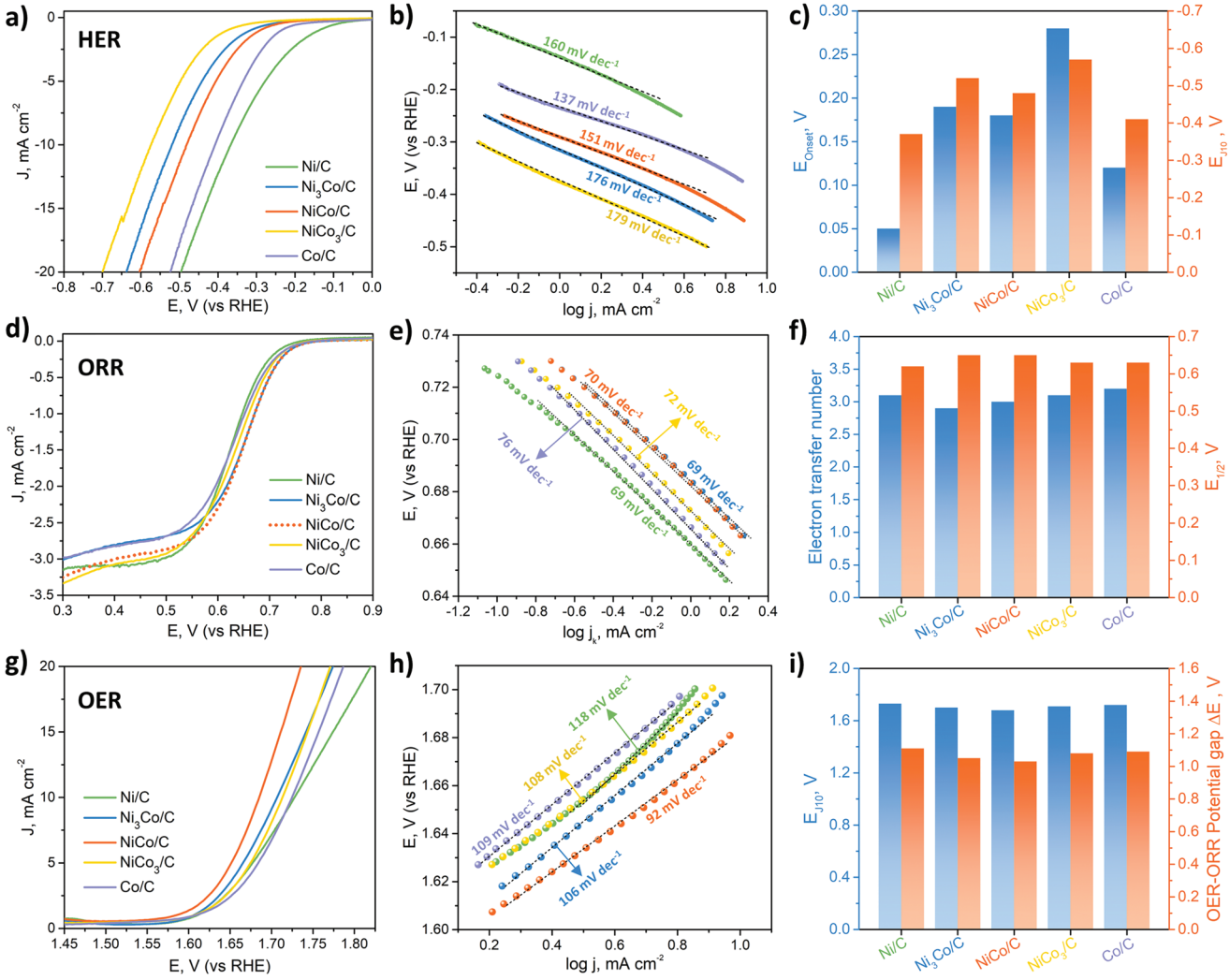

Figure 6. The HER, ORR, and OER performance of Ni/C, Ni_3Co/C, NiCo/C, $NiCo_3/C$, and Co/C catalysts: a) HER LSV curves, b) HER Tafel plots, c) comparison of E_{onset} and E_{J10} of different catalysts. d) ORR LSV curves, e) ORR Tafel plots, and f) comparison of electron transfer number and $E_{1/2}$ of different catalysts. g) OER LSV curves, h) OER Tafel plots, and i) comparison of E_{J10} and ΔE of different catalysts. All the polarization curves were recorded in 0.1 M KOH electrolyte at a rotating speed of 1600 rpm on rotating disk electrode (RDE) with the scan rates of 10 mV s^{-1}. O_2-saturated electrolyte was used to obtain the ORR and OER LSV curves, while HER LSV curve was recorded in N_2-saturated electrolyte.

2.3.3. OER

To evaluate the OER performance of the catalysts, LSV was carried out in the potential window of 1.0–2.0 V to obtain the polarization curves (Figure 6g). Similar to HER, the E_{J10} value was also a crucial parameter to evaluate the OER performance.[58] As displayed in Figure 6i, the NiCo/C sample possesses the smallest E_{J10} value (1.68 V), indicating its superior OER performance among the studied catalysts. In addition, as seen in Figure 6h, the smallest Tafel plot value, 92 mV dec^{-1}, belongs to the NiCo/C, which indicates a faster electrokinetic of the water oxidation process on the surfaces of NiCo/C.[59] The potential gap (ΔE) between the ORR half-wave potential ($E_{1/2}$) and OER potential (E_{J10}) is used as a common criterion for evaluating the overall bifunctional activity.[56,60] Figure 6i displays the ΔE values of the five samples. As seen in the figure, NiCo/C possesses the smallest ΔE (1.03 V), indicating its best performance as a bifunctional ORR/OER catalyst for the metal–air battery.

2.3.4. Electrocatalytic Performance Versus Catalysts' Composition

The relationship between the catalysts' compositions and their electrocatalytic performance was established and shown in Figure 7a–c. The specific activity of the catalysts for HER, ORR, and OER at a typical operating overpotential (η = 500 mV) are plotted as a function of the Co atomic faction in the catalysts. Note that, the electrochemical surface area (ESA) of the catalysts was determined by the double-layer capacitance (C_{dl}) method.[30,58] C_{dl} was measured from current-scan rates via cyclic voltammetry (CV) in the non-Faraday region (Figure S7a–e, Supporting Information) for all studied catalysts (Figure S7f, Supporting Information). ESA was found to be 4.8, 7.0, 8.5, 7.8,

ADVANCED MATERIALS INTERFACES
Open Access
www.advmatinterfaces.de

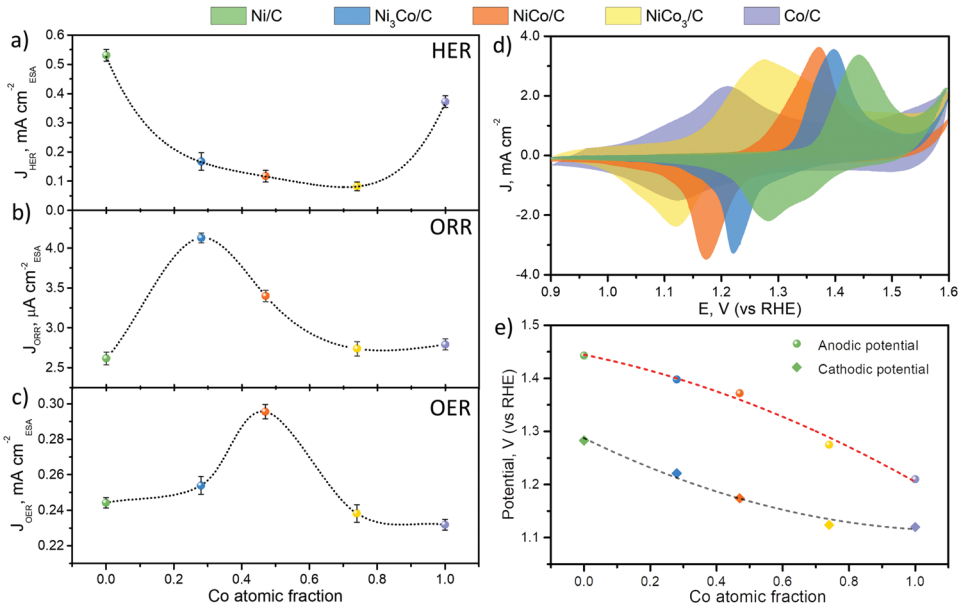

Figure 7. Specific activity, of the Co–Ni catalysts for a) HER, b) ORR, and c) OER, in alkaline solutions as a function of Co atomic fraction. The specific activities were calculated at the overpotentials of $\eta = 500$ mV for all three reactions (ORR = 0.723 V, HER = 0.500 V, and OER = 1.723 V vs RHE). d) CV curves recorded in 0.1 M N_2 saturated KOH solution at a scan rate of 50 mV s^{-1}. e) Polynomial-fitted anodic/cathodic potentials as the function of Co content (mole percentage). Dashed lines are guides to eyes.

and 6.3 cm^2 for Ni/C, Ni_3Co/C, NiCo/C, $NiCo_3$/C, and Co/C, respectively. As shown in the figure, the catalytic activities toward ORR (Figure 7b) and OER (Figure 7c) exhibit a volcano-like dependence on the composition of catalysts. Specifically, Ni_3Co/C and NiCo/C possess the highest specific activities for ORR and OER, respectively. Meanwhile, a reverse trend is observed in the HER activity of the catalysts (Figure 7a). Thus, both monometallic Ni/C and Co/C catalysts show prominent HER specific activity. At the same time, the HER specific activity of the $NiCo_3$/C catalyst is the lowest. Based on the specific activity result, it becomes clear that the variation of the composition in the catalysts can tune their catalytic activities.

As all reactions occur on the surface of the catalysts, cyclic voltammetry measurements were performed to verify the surface composition. As shown in the literature, in alkaline solutions, metallic Ni° can be converted to $Ni(OH)_2$ at the electrode as a result of spontaneous oxidation and hydration process ($Ni \rightarrow NiO \rightarrow Ni(OH)_2$).[61,62] Similar transformation was found for Co ($Co \rightarrow CoO_x \rightarrow Co(OH)_2$).[63] From the XPS analysis, we know that the surface of the catalysts prior to the electrochemical test is covered by (hydro)oxides (M^{2+}). Therefore, the CV curves display a pair of well-defined redox peaks that correspond to the reversible conversion between Ni^{2+} and Ni^{3+} for Ni-containing samples and between Co^{2+} and Co^{3+} for Co-containing samples. It should be noted that, for the monometallic Co/C sample, besides the redox peak at ≈1.15/1.2 V, there is another pair peak appearing at ≈1.50/1.55 V; this peak may correspond to the redox pair Co^{3+}/Co^{4+}.[64] As seen in Figure 7d, when the Co content in the alloy samples increases, the redox potential of $Ni^{2+/3+}$ wave shifts to lower potentials. Meanwhile, a reverse trend is observed for the redox potential of $Co^{2+/3+}$. This shift may be ascribed to the interactions between the Co and Ni that modifies the electronic structure of material upon alloying.[65] The trend of the redox potential shifts may indicate the level of difficulty of transitions from M^{2+} to M^{3+}.[65] For instance, one can expect that the more Co is present in the Co–Ni alloy, the more difficult it is to oxidize Ni^{2+} to Ni^{3+}. Tuning of the redox potential in the 3d-metal catalysts is widely used for improving the performance of oxygen electrocatalysis.[66]

2.4. Factors That Influence Catalytic Activity of Ni(Co)

It was found that, the catalytic activity of the nanomaterials obtained in the current study is strongly dependent on their structure and composition. Note that the physical and chemical properties of all catalysts studied here retain both similarity and differences. Thus, all of them i) are deposited on commercial carbon Vulcan XC-72 as support; ii) the NPs in all the samples can be divided into two fractions based on their size: small particles (1–3 nm) incorporated into the carbon support and large particles (10–40 nm) distributed on the carbon; iii) small particles can be fully oxidized, and some larger ones contain the non-stoichiometric oxide on their surfaces. At the same time, the redox potentials/oxidation capability of Ni^{2+} (Co^{2+}), the energy of the defect (twin boundaries) formation, and the catalytic performance of the samples are found to be dependent on the Ni–Co alloy composition.

2.4.1. HER Activity

As seen in Figure 7a, both monometallic samples exhibit higher HER activity as compared to the alloyed catalysts (the minimum current density is registered in $NiCo_3$/C). At the

same time, it is surprising that this activity is highest in the Ni/C sample. Markovic et al. used OH—$M^{2+\delta}$ (M is a 3d transition metal) bond strength ($0 \leq \delta \leq 1.5$) as a descriptor for the water electrolyser reactions.[67] The authors found that the bond strength of OH—$Ni^{2+\delta}$ is weaker than OH—$Co^{2+\delta}$, and the reactivity of the corresponding catalysts shows the inverse trend: Ni hydr(oxy)oxide is more reactive than Co hydr(oxy)oxide. Thus, the observed HER activity of the monometallic Ni/C and Co/C catalysts could be explained by the difference in the OH—$M^{2+\delta}$ bond strength. At the same time, we observe that the alloying of Ni and Co does not contribute much to the HER activity of the Ni–Co samples. Considering the low HER potential region ($E < 0.0$ V vs RHE), both Ni and Co maintain only the valence state of ≈+2,[67] and, as described above, they may exist as $Ni(OH)_2$ and/or $Co(OH)_2$ on the surface of the catalysts in the full HER test potential region. As it was reported previously. in an alkaline HER, the Volmer step of water dissociation is crucial and it limits the activity of Pt and Pt-group metals (PGM)[67,68] A lot of work has been done to improve the efficiency of the catalysts by creating a bifunctional 3d-metal hydr(oxy)oxide-PGM system. 3d-metal hydr(oxy)oxides are more efficient for cleaving HO—H bonds due to the fact that they favor the generation of the hydrogen intermediates (H_{ad}) on the surfaces. The higher activity of Ni/C and Co/C, compared to the alloy samples, might be attributed to the higher efficiency of water dissociation on the $Ni(OH)_2$ and $Co(OH)_2$ rather than on the Ni–Co hydr(oxy)oxide complex. Note that Co/C and NiCo/C show much lower Tafel slope values compared with the other samples (see Figure 6b). It may indicate that the reaction kinetics in these samples is somehow faster than in the other catalysts. This may be due to the higher density of defects in the Co/C and NiCo/C samples, which provide additional active sites.

2.4.2. ORR and OER Activity

As seen in Figure 7b,c, where ORR and OER activity is plotted as a function of cobalt content, the specific activity of the catalysts displays a volcano tendency and the best ORR and OER catalysts are Ni_3Co/C and NiCo/C, respectively. Moreover, NiCo/C, being an OER superior catalyst, has also been proven to have a high concentration of defects. Santiago et al. in the report on bimetallic NiCu catalysts, found that the surface defects in the nanoalloy material reduce the uphill energy states at each step of the OER process.[59] Surface defects are also reported to be responsible for the enhanced OER activity in other Ni-based catalysts.[69,70] The low Tafel slope values measured for the NiCo/C sample also confirm its improved OER kinetics, which might be attributed to the presence of defects. In addition, in the OER potential region (1.0–1.8 V), the oxidation ability of Ni^{2+} and Co^{2+} in the NiCo/C sample may reach equilibrium; and therefore, some $Ni_xCo_yO_z$ compounds may form on the electrode surface. It has been reported that materials containing $Ni_xCo_yO_z$ show high activity to OER.[71,72] Regarding ORR, although Ni_3Co/C catalyst exhibits a superior specific activity, the ORR efficiency of all five studied catalysts is quite close to each other. Note that, the values of current density in Figure 7b are in the microamp range. Moreover, the Tafel slope values are also similar, indicating very similar ORR kinetics. Electron transfer numbers for all the samples are close to 3 rather than the desired four-electron transfer. Therefore, the correlation between the composition of the Ni–Co alloy samples and their ORR performance would not be that straightforward in this case.

Compared to commercial and state-of-the-art catalysts described in the literature, the studied Ni–Co/C catalysts do not show significant electrocatalytic activities for HER, ORR, or OER.[73–76] However, their overall catalytic performance reaches the same level as that of Ni–Co nanoparticle catalysts on a non-functionalized commercial carbon as a support, reported in the literature.[9] Indeed, the use of transition metal non-oxide electrocatalysts is still the subject of fundamental research and yet to be commercialized for practical applications.[75] In the current study, Ni–Co nanocatalysts were deposited on non-functionalized commercial carbon to minimize contribution to the electrocatalytic activity from the supporting material. Therefore, the effect of composition and stacking faults of Ni–Co nanoparticles on their trifunctional activity was revealed: the structural defects may strongly affect the electrochemical performance of the catalyst toward OER; this effect is less pronounced with respect to ORR, while for HER, the role of defects is insignificant. The results presented in our study can be used to develop more active NiCo-based catalysts by combing conventionally used strategies, such as doping, nanostructure engineering, and the use of suitable support materials.

3. Conclusion

Ni–Co alloy nanoparticles with various Co-to-Ni ratios from 0 to 1, were obtained by the γ-radiation-induced reduction, Co^{2+}(Ni^{2+}) to Co(Ni), from a mixture of aqueous solutions of Ni and Co acetates (precursors). The nanoparticles were deposited directly on the carbon support during the synthesis. The structural, chemical, and electrochemical properties (activity toward HER, ORR, and OER) of the obtained samples were investigated aiming to reveal the effect of the composition of alloys on their properties.

The following findings are emphasized:

1. During the synthesis of Ni–Co nanoparticles, the presence of cobalt in the reaction solutions inhibits the backwords reactions, that leads to re-oxidation of reduced nickel. This is confirmed by the fact that the conversion yield of Ni^{2+} to Ni increases when cobalt precursor is added to solutions.
2. TEM analysis reveals that the two types of Ni–Co/C nanoparticles are present in the studied samples: i) small particles (1–3 nm) tightly incorporated into the carbon support and ii) large clusters (10–40 nm) distributed on the carbon. Depending on the size, these nanoparticles can be partially or fully oxidized forming corresponding Ni(Co) oxides/hydroxides, as confirmed by XES, XAS, XPS, and TEM studies.
3. As follows from ab initio calculations and confirmed by XRD and TEM studies, all samples have close-packed structures with structural defects in the form of stacking faults. The concentration of these defects reaches the maximum in the alloy sample where Ni-to-Co ratio is close to 1. These defects may play dominating role in the increased catalytic activity of the NiCo/C sample toward OER.

4. The electrocatalytic activity of the Ni–Co/C nanoparticles toward HER, OER, and ORR is affected by the alloy content. Thus, ORR and OER activity is increased in the alloy samples, Ni_3Co/C and NiCo/C, respectively. Meanwhile, HER activity reaches its maximum in the Ni/C samples. The latter may be attributed to the change in the 3d metal—OH bond strengths upon alloying.

Our study demonstrates that the composition of Ni–Co-based nanocatalysts is an essential factor having an impact on their structure and electrochemical performance with respect to various catalytic reactions.

4. Experimental Section

Chemicals: Nickel (II) acetate tetrahydrate, $Ni(CH_3COO)_2{\cdot}4H_2O$ (98%), Cobalt (II) acetate tetrahydrate, $Co(CH_3COO)_2{\cdot}4H_2O$ (98%), propan-2-ol, and $(CH_3)_2CHOH$ (IPA, 99.9%) were purchased from Sigma–Aldrich. Carbon black and Vulcan XC-72 were from Cabot Carbon Corporation, USA. Milli-Q water (Millipore, 18.2 MΩ cm at 25 °C) was used in all experiments.

Synthesis Conditions: All the samples were prepared by γ-radiation induced synthesis method where a Cs-137 (MDS Nordion 1000 Elite) was used as a gamma source. The total irradiation dose was controlled by the time of the samples' exposure to irradiation. The dose rate estimated with ferrous sulfate (Fricke) dosimetry, was 0.15 Gy s^{-1}. Isopropanol (IPA) was added as an OH radicals' scavenger and carbon black Vulcan XC-72 was used as a support. Specifically, to synthesize the alloy with Ni-to-Co ratio equal to 1 on carbon support, NiCo/C (35 mg) of carbon black Vulcan XC-72 was added to a mixture of IPA (9 mL) and H_2O (19.4 mL) and kept in an ultrasonic bath for 10 min. $Ni(CH_3COO)_2{\cdot}4H_2O$ (0.8 ml, 0.1 M) and $Co(CH_3COO)_2{\cdot}4H_2O$ (0.8 ml, 0.1 M) were then added dropwise to the carbon suspension. The mixture was placed into an ultrasonic bath again for 30 min and then stirred at 1000 RPM for another 2 h. Prior to irradiation, the mixture was purged with N_2 for 30 min and sealed with septum in glass vials. The irradiation time was 48 h for all the samples which correspond to the total dose of 26 kGy. The initial pH of all the sample solutions was ≈7; after irradiation, pH decreased to ≈5.5. After irradiation, the precipitates were separated from the solutions by using a magnet. The precipitate extraction was done in a glovebox under an Ar atmosphere (oxygen content < 0.1 ppm). The products were then washed with deaerated MilliQ water twice and then dried in the glove box. By varying the relative amount of Ni^{2+} and Co^{2+} precursors, Ni/C, Ni_3Co/C, $NiCo_3/C$, and Co/C were prepared following the same procedure as that for NiCo/C. The total concentration of metal ions precursors for all the samples was kept constant and equal to 5.5 mM. IPA concentration was 2 M. The total absorbed dose of 26 kGy allowed the full conversion of Ni^{2+} (Co^{2+}) ions into the corresponding atom, Thus, the expected amount of Ni (Co) on carbon was 20 wt%.

Analytical Methods: X-ray diffraction (XRD) measurements were carried out using a PANalytical X'Pert PRO diffractometer in Bragg–Brentano geometry with CuKα radiation at a wavelength $\lambda = 1.54$ Å.

The amount of Ni–Co on carbon (actual metal loading) and the catalyst ink concentration was determined by inductively coupled plasma-optical emission spectroscopy (ICP-OES) with a Thermo scientific iCAP 600 series instrument. The samples were digested in 10% nitric acid overnight with 30 min of ultrasonic microwave assisted extraction.

X-ray photo electron spectroscopy (XPS) spectra were recorded with a Kratos Axis Ultra electron spectrometer with a delay line detector. A monochromatic Al Kα source operated at 150 W, a hybrid lens system with a magnetic lens, providing an analyzed area of 0.3×0.7 mm^2, and a charge neutralizer were used for the measurements. The base pressure in the analysis chamber was below 3×10^{-9} Torr. The binding energy (BE) scale was referenced to the C 1s of aliphatic carbon, set at 285.0 eV.

Transmission electron microscopy (TEM) measurements were performed using an FEI Tecnai G2 F20 operating at 200 kV and a double Cs corrected JEOL JEM-ARM200F (S)TEM operated at 80 kV equipped with a cold-field emission gun and a high-angle silicon drift energy dispersive X-ray (EDX) detector (solid angle up to 0.98 steradians with a detection area of 100 mm^2). Annular dark-field scanning transmission electron microscopy (ADF-STEM) images were collected at a probe convergence semi-angle of 25 mrad.

X-ray absorption (XAS) and X-ray emission (XES) measurements were performed at the BM20 ROBL beamline[77] at the European synchrotron radiation facility (ESRF, Grenoble, France). The high energy resolution fluorescence detected X-ray absorption spectroscopy (HERFD-XAS) and XES data were collected at room temperature using a Johann-type X-ray emission spectrometer in a vertical Rowland geometry.[78] More details about the measurement can be found in the Supporting Information.

Electrochemical characterization was conducted in a three-electrode system using a potentiostat (EG&G Model 363A) with a Hg/HgO (1.0 M KOH as filling solution) as a reference electrode and a graphite rod as a counter electrode. Details about the catalyst ink and thin film working electrode preparation are described in the Supporting Information. The catalytic properties of the catalysts were investigated for trifunctional HER, ORR, and OER in KOH (0.1 M). All the potentials reported here were iR-corrected and calibrated to a reversible hydrogen electrode (RHE) according to E(RHE) = E(Hg/HgO) + 0.865 V in KOH (0.1 M).

Supporting Information

Supporting Information is available from the Wiley Online Library or from the author.

Acknowledgements

Y.Y. and I.L.S. acknowledge financial support from the Swedish Foundation for Strategic Research, SSF (Grant EM16-0060). Andrey Shchukarev, Department of Chemistry, Umeå University, is acknowledged for performing XPS characterization. Ceshigou Research Service, China, is acknowledged for the magnetic characterization of samples. The computations were enabled by resources provided by the National Academic Infrastructure for Supercomputing in Sweden (NAISS) and the Swedish National Infrastructure for Computing (SNIC) at PDC Center for High Performance Computing, Stockholm, partially funded by the Swedish Research Council, VR, grant numbers 2022-06725 and 2018-05973.

Conflict of Interest

The authors declare no conflict of interest.

Author Contributions

Y.Y. and I.L.S. conceived the project and were responsible for structuring the manuscript, collecting the results, and compiling the final version of the manuscript. Y.Y. performed synthesis of the samples and their structural and electrochemical characterization. P.A.K. performed ab initio calculations and analysis of the results. P.A.N. calculated chemical and electrochemical equilibria of Ni–Co–Acetate–H_2O system. E.F.B., K.O.K., and S.M.B. performed XAS and XES experiments and data analysis. N.V.T. contributed to electron microscopy experiments, data processing, and description of the results. All authors participated in discussion of the results and contributed to the manuscript preparation.

ADVANCED MATERIALS INTERFACES
Open Access
www.advmatinterfaces.de

Data Availability Statement

The data that support the findings of this study are available from the corresponding author upon reasonable request.

Keywords

electrocatalytic performance, gamma-radiolytic reduction, Ni–Co nanocatalysts, stacking faults defects

Received: January 13, 2023
Revised: April 7, 2023
Published online: May 12, 2023

[1] Z. W. Seh, J. Kibsgaard, C. F. Dickens, I. Chorkendorff, J. K. Nørskov, T. F. Jaramillo, *Science* **2017**, *355*, eaad4998.
[2] J. Suntivich, H. A. Gasteiger, N. Yabuuchi, H. Nakanishi, J. B. Goodenough, Y. Shao-Horn, *Nat. Chem.* **2011**, *3*, 546.
[3] J. W. D. Ng, M. Tang, T. F. Jaramillo, *Energy Environ. Sci.* **2014**, *7*, 2017.
[4] Y.-L. Zhang, K. Goh, L. Zhao, X.-L. Sui, X.-F. Gong, J.-J. Cai, Q.-Y. Zhou, H.-D. Zhang, L. Li, F.-R. Kong, D.-M. Gu, Z.-B. Wang, *Nanoscale* **2020**, *12*, 21534.
[5] Q. Pan, L. Wang, *J. Power Sources* **2021**, *485*, 229335.
[6] M. S. Burke, L. J. Enman, A. S. Batchellor, S. Zou, S. W. Boettcher, *Chem. Mater.* **2015**, *27*, 7549.
[7] F. Arshad, T. ul Haq, A. Khan, Y. Haik, I. Hussain, F. Sher, *Energy Convers. Manage.* **2022**, *254*, 115262.
[8] W. Zhou, H. Su, S. Shen, Y. Li, H. Zhang, M. Liu, X. Zhao, W. Cheng, P. Yao, Q. Liu, *ACS Sustainable Chem. Eng.* **2020**, *8*, 6898.
[9] Y.-C. Zhang, C. Han, J. Gao, L. Pan, J. Wu, X.-D. Zhu, J.-J. Zou, *ACS Catal.* **2021**, *11*, 12485.
[10] R. Ferrando, J. Jellinek, R. L. Johnston, *Chem. Rev.* **2008**, *108*, 845.
[11] Y. Li, G. A. Somorjai, *Nano Lett.* **2010**, *10*, 2289.
[12] J. Zhang, H. Wang, A. K. Dalai, *J. Catal.* **2007**, *249*, 300.
[13] O. Ergeneman, K. M. Sivaraman, S. Pané, E. Pellicer, A. Teleki, A. M. Hirt, M. D. Baró, B. J. Nelson, *Electrochim. Acta* **2011**, *56*, 1399.
[14] H. Li, J. Liao, Y. Feng, S. Yu, X. Zhang, Z. Jin, *Mater. Lett.* **2012**, *67*, 346.
[15] R. Brayner, M. J. Vaulay, F. Fiévet, T. Coradin, *Chem. Mater.* **2007**, *19*, 1190.
[16] D. I. Klimov, E. A. Zezina, S. B. Zezin, M. Yang, F. Wang, V. I. Shvedunov, V. I. Feldman, A. A. Zezin, *Radiat. Phys. Chem.* **2018**, *142*, 65.
[17] J. L. Marignier, J. Belloni, M. O. Delcourt, J. P. Chevalier, *Nature* **1985**, *317*, 344.
[18] J. Belloni, *Catal. Today* **2006**, *113*, 141.
[19] J. Belloni, M. Mostafavi, H. Remita, J. L. Marignier, M. O. Delcourt, *New J. Chem.* **1998**, *22*, 1239.
[20] I. L. Soroka, N. V. Tarakina, A. Hermansson, L. Bigum, R. Widerberg, M. S. Andersson, R. Mathieu, A. R. Paulraj, Y. Kiros, *Dalton Trans.* **2017**, *46*, 9995.
[21] X. Yuan, D. Dragoe, P. Beaunier, D. B. Uribe, L. Ramos, M. G. Méndez-Medrano, H. Remita, *J. Mater. Chem. A* **2020**, *8*, 268.
[22] C. Dispenza, N. Grimaldi, M. A. Sabatino, I. L. Soroka, M. Jonsson, *J. Nanosci. Nanotechnol.* **2015**, *15*, 3445.
[23] M. Treguer, C. De Cointet, H. Remita, J. Khatouri, M. Mostafavi, J. Amblard, J. Belloni, R. De Keyzer, *J. Phys. Chem. B* **1998**, *102*, 4310.
[24] C. M. Doudna, M. F. Bertino, S. Pillalamarri, F. D. Blum, A. T. Tokuhiro, S. Chattopadhyay, J. Terry, *MRS Proc.* **2002**, *740*, I11.2.
[25] C. De Cointet, M. Mostafavi, J. Khatouri, J. Belloni, *J. Phys. Chem. B* **1997**, *101*, 3512.
[26] H. Remita, A. Etcheberry, J. Belloni, *J. Phys. Chem. B* **2003**, *107*, 31.
[27] A. Henglein, M. Giersig, *J. Phys. Chem.* **1994**, *98*, 6931.
[28] Y. Yang, G. Montserrat-Sisó, B. Wickman, P. A. Nikolaychuk, I. L. Soroka, *Dalton Trans.* **2022**, *51*, 3604.
[29] Y. Yang, I. L. Soroka, *ChemCatChem* **2022**, 14, 202200941.
[30] Y. Yang, M. Johansson, A. Wiorek, N. V. Tarakina, F. Sayed, R. Mathieu, M. Jonsson, I. L. Soroka, *Dalton Trans.* **2021**, *50*, 376.
[31] R. M. Bozorth, *Ferromagnetism*, IEEE Press, New York, NY **1993**.
[32] L. Wang, Y. Gao, Q. Xue, H. Liu, T. Xu, *Appl. Surf. Sci.* **2005**, *242*, 326.
[33] N. Wang, T. Hang, S. Shanmugam, M. Li, *CrystEngComm* **2014**, *16*, 6937.
[34] X. Gao, Y. Yu, Q. Liang, Y. Pang, L. Miao, X. Liu, Z. Kou, J. He, S. J. Pennycook, S. Mu, J. Wang, *Appl. Catal., B* **2020**, *270*, 118889.
[35] D. Ung, G. Viau, F. Fiévet-Vincent, F. Herbst, V. Richard, F. Fiévet, *Prog. Solid State Chem.* **2005**, *33*, 137.
[36] M. Cheng, M. Wen, S. Zhou, Q. Wu, B. Sun, *Inorg. Chem.* **2012**, *51*, 1495.
[37] A. V. Rudnev, A. S. Lysakova, P. E. Plyusnin, Y. I. Bauman, Y. V. Shubin, I. V. Mishakov, A. A. Vedyagin, R. A. Buyanov, *Inorg. Mater.* **2014**, *50*, 566.
[38] J. W. T. Spinks, R. J. Woods, *An Introduction to Radiation Chemistry*, John-Wiley & Sons, Inc., 3rd ed., New York, Toronto **1990**.
[39] *CRC Handbook of Chemistry and Physics* (Ed.: D. R. Lide), CRC Press, Boca Raton, FL **2007**.
[40] Z. Li, M. Jonsson, *Carbon* **2021**, *173*, 61.
[41] A. W. Hull, *Phys. Rev.* **1921**, *17*, 571.
[42] D. Pandey, P. Krishna, *Prog. Cryst. Growth Charact.* **1983**, *7*, 213.
[43] G. Carturan, G. Cocco, S. Enzo, R. Ganzerla, M. Lenarda, *Mater. Lett.* **1988**, *7*, 47.
[44] T. J. Kühn, J. Hormes, N. Matoussevitch, H. Bönnemann, P. Glatzel, *Inorg. Chem.* **2014**, *53*, 8367.
[45] S. C. Chou, K. C. Tso, Y. C. Hsieh, B. Y. Sun, J. F. Lee, P. W. Wu, *Materials* **2020**, *13*, 2703.
[46] Y. Jia, K. Jiang, H. Wang, X. Yao, *Chem* **2019**, *5*, 1371.
[47] G. C. Trigunayat, A. R. Verma, in *Crystallography and Crystal Chemistry of Materials With Layered Structures* (Ed: F. Lévy), Springer Netherlands, Dordrecht, The Netherlands **1976**, p. 269.
[48] A. Guinier, G. B. Bokij, K. Boll-Dornberger, J. M. Cowley, S. Durovič, D. E. Cox, H. Jagodzinski, P. Krishna, P. M. De Wolff, B. B. Zvyagin, P. Goodman, T. Hahn, K. Kuchitsu, S. C. Abrahams, *Acta Crystallogr., Sect. A: Found. Adv.* **1984**, *40*, 399.
[49] L. Vitos, *Phys. Rev. B* **2001,** *64*, 014107.
[50] L. Vitos, *Computational Quantum Mechanics for Materials Engineers: The EMTO Method and Applications*, Springer, London **2007**, pp. 83–94.
[51] W. Selke, *Phys. Rep.* **1988**, *170*, 213.
[52] A. Y. Faid, F. Foroughi, S. Sunde, B. Pollet, *J. Appl. Electrochem.* **2022**, *52*, 1819.
[53] T. Shinagawa, A. T. Garcia-Esparza, K. Takanabe, *Sci. Rep.* **2015**, *5*, 13801.
[54] Z. Li, Y. Yang, A. Relefors, X. Kong, G. M. Siso, B. Wickman, Y. Kiros, I. L. Soroka, *J. Colloid Interface Sci.* **2021**, *583*, 71.
[55] J. Wang, Z. Wu, L. Han, R. Lin, H. L. Xin, D. Wang, *ChemCatChem* **2016**, *8*, 736.
[56] Z. F. Huang, J. Wang, Y. Peng, C. Y. Jung, A. Fisher, X. Wang, *Adv. Energy Mater.* **2017**, *7*, 1700544.
[57] D. A. Walsh, A. Ejigu, J. Smith, P. Licence, *Phys. Chem. Chem. Phys.* **2013**, *15*, 7548.
[58] C. C. L. McCrory, S. Jung, J. C. Peters, T. F. Jaramillo, *J. Am. Chem. Soc.* **2013**, *135*, 16977.
[59] M. A. Ahsan, A. R. Puente Santiago, Y. Hong, N. Zhang, M. Cano, E. Rodriguez-Castellon, L. Echegoyen, S. T. Sreenivasan, J. C. Noveron, *J. Am. Chem. Soc.* **2020**, *142*, 14688.
[60] C. X. Zhao, J. N. Liu, J. Wang, D. Ren, J. Yu, X. Chen, B. Q. Li, Q. Zhang, *Adv. Mater.* **2021**, *33*, 2008606.

ADVANCED MATERIALS INTERFACES
Open Access
www.advmatinterfaces.de

[61] C.-W. Kung, Y.-H. Cheng, K.-C. Ho, *Sens. Actuators, B* **2014**, *204*, 159.
[62] Y. Yang, G. Montserrat-sisó, B. Wickman, P. A. Nikolaychuk, I. L. Soroka, *Dalton Trans.* **2022**, *51*, 3604.
[63] K. M. Ismail, W. A. Badawy, *J. Appl. Electrochem.* **2000**, *30*, 1303.
[64] H. Yang, F. Li, S. Zhan, Y. Liu, W. Li, Q. Meng, A. Kravchenko, T. Liu, Y. Yang, Y. Fang, L. Wang, J. Guan, I. Furó, M. S. G. Ahlquist, L. Sun, *Nat. Catal.* **2022**, *5*, 414.
[65] M. S. Burke, M. G. Kast, L. Trotochaud, A. M. Smith, S. W. Boettcher, *J. Am. Chem. Soc.* **2015**, *137*, 3638.
[66] D. A. Kuznetsov, B. Han, Y. Yu, R. R. Rao, J. Hwang, Y. Román-Leshkov, Y. Shao-Horn, *Joule* **2018**, *2*, 225.
[67] R. Subbaraman, D. Tripkovic, K. C. Chang, D. Strmcnik, A. P. Paulikas, P. Hirunsit, M. Chan, J. Greeley, V. Stamenkovic, N. M. Markovic, *Nat. Mater.* **2012**, *11*, 550.
[68] N. Danilovic, R. Subbaraman, D. Strmcnik, K. C. Chang, A. P. Paulikas, V. R. Stamenkovic, N. M. Markovic, *Angew. Chem., Int. Ed.* **2012**, *51*, 12495.
[69] Z. R. Ramadhan, A. R. Poerwoprajitno, S. Cheong, R. F. Webster, P. V. Kumar, S. Cychy, L. Gloag, T. M. Benedetti, C. E. Marjo, M. Muhler, D. W. Wang, J. J. Gooding, W. Schuhmann, R. D. Tilley, *J. Am. Chem. Soc.* **2022**, *144*, 11094.
[70] L. Lei, D. Huang, M. Cheng, R. Deng, S. Chen, Y. Chen, W. Wang, *Coord. Chem. Rev.* **2020**, *418*, 213372.
[71] Y. Ha, L. Shi, X. Yan, Z. Chen, Y. Li, W. Xu, R. Wu, *ACS Appl. Mater. Interfaces* **2019**, *11*, 45546.
[72] S. V. Devaguptapu, S. Hwang, S. Karakalos, S. Zhao, S. Gupta, D. Su, H. Xu, G. Wu, *ACS Appl. Mater. Interfaces* **2017**, *9*, 44567.
[73] C. Wei, R. R. Rao, J. Peng, B. Huang, I. E. L. Stephens, M. Risch, Z. J. Xu, Y. Shao-Horn, *Adv. Mater.* **2019**, *31*, 1806296.
[74] F. Ganci, V. Cusumano, P. Livreri, G. Aiello, C. Sunseri, R. Inguanta, *Int. J. Hydrogen Energy* **2021**, *46*, 10082.
[75] C. Das, N. Sinha, P. Roy, *Small* **2022**, *18*, 2202033.
[76] X. Liu, M. Park, M. G. Kim, S. Gupta, G. Wu, J. Cho, *Angew. Chem., Int. Ed.* **2015**, *54*, 9654.
[77] A. C. Scheinost, J. Claussner, J. Exner, M. Feig, S. Findeisen, C. Hennig, K. O. Kvashnina, D. Naudet, D. Prieur, A. Rossberg, M. Schmidt, C. Qiu, P. Colomp, C. Cohen, E. Dettona, V. Dyadkin, T. Stumpf, *J. Synchrotron Radiat.* **2021**, *28*, 333.
[78] K. O. Kvashnina, A. C. Scheinost, *J. Synchrotron Radiat.* **2016**, *23*, 836.